33RD CONGRESS
OF THE INTERNATIONAL COUNCIL
OF THE AERONAUTICAL SCIENCES
STOCKHOLM, SWEDEN, 4-9 SEPTEMBER, 2022

ICAS 2022 SWEDEN

Some Experimental Results on Dynamic Aeroelasticity of Plates and Shells in Subsonic and Supersonic Flow.

Jannis Lübker[1]

[1]jannisluebker@gmail.com

Abstract

Shells and plates exposed to supersonic flow can be subject to dynamic aeroelastic instability called panel flutter, which is caused by the elimination of the system's damping. This is initiated by aerodynamic loads induced by initial structural motions. Experimental activities on this subject were performed by DLR Institute for Aeroealsticity at DNW Transonic Wind Tunnel in Göttingen on rectangular and flat plates. Besides the aerodynamic parameters Mach number and Reynolds number, structural parameters, such as amplitude and excitation frequency, were varied for two simulated modal shapes by means of a forced excitation approach. Unsteady pressure and deformation measurements were done in order to determine the local aerodynamic responses evoked by the structure's oscillating deformation and based on that Generalized Aerodynamic Forces. The excerpt of those tests that is presented in this paper focuses on the Mach number's impact, which is varied in a range of $0.7 < M_\infty < 1.2$, on the pressure response and the resulting aerodynamic damping. For validation analytic approaches for high supersonic and low subsonic flow conditions are applied. Elaborate knowledge about the non-linear aeroelastic behaviour in the high subsonic and low supersonic flow domain may lead the way to less conservative designed and thus light weight designed aerospace structures. A contribution to sustainability follows due to resulting savings in mass and fuel.

Keywords: Measurement technique, Aeroelasticity, Wind Tunnel, Panel flutter, Subsonic/Supersonic flow

Nomenclatur

Latin

$\widehat{A}$	=	Amplitude of Oscillation
a	=	*Length*
b	=	*Width*
c_p	=	Pressure Coefficient
D	=	Plate Bending Stiffness
E	=	Young's Modulus
d	=	Time depending z-Deflection
f_{exc}	=	Excitation Frequency
h	=	Panel Thickness
$\Im$	=	Imaginary Part of a Complex Number
J	=	Geometrical Moment of Inertia
l	=	Length
n	=	Plate Bending Mode Number
t	=	Time
M_∞	=	Free Stream Mach number
p	=	Pressure
$\Re$	=	Real Part of a Complex Number
U_∞	=	Free Stream Velocity
W	=	Width
x	=	x-Coordinate
y	=	y-Coordinate
z	=	z-Coordinate

Greek

ϕ	=	Phase Angle
ρ_s	=	Structure Density
ψ	=	Eigenfunction
ω	=	Angular Frequency

Abbreviations

CFD	Computational Fluid Dynamics
DNW	German Dutch Wind Tunnels
DOF	Degree of Freedom
FEM	Finite Element Method
GAF	Generalized Aerodynamic Forces
LCO	Limit Cycle Oscillation
MAC	Modal Assurance Criterion
SPR	Stereo Pattern Recognition
TWG	Transonic Wind Tunnel Göttingen

1. Introduction

In the scope of the US spaceflight programs and the connected first manned moon landing of the Apollo 11 mission extensive investigations were carried out on a aeroelastic phenomenon known as panel flutter, investigated in the mid 1940s, which arises due to the interaction between thin shell and plate structures and flowing fluid. In supersonic flow those structures, which are exposed to the flow on one side, can undergo self excited oscillations caused by the aerodynamic response induced by the structure's motion. Figure 1 shows a simple model according to Dowell [1] with a plate of length *a,* that has clamped mechanical boundary conditions on leading edge and trailing edge. The plate is exposed to a flow M_∞ that has a boundary layer that is not considered in this paper. The shown oscillating motion of the structure is the first modal shape of a clamped beam.

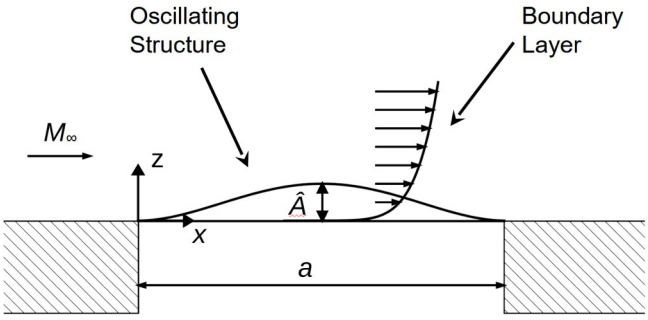

Figure 1 – Panel flutter model.

In case of arising oscillations of the structure, these are of a limit cycle type that eventually leads to the plate's failure due to fatigue [2]. Among others, important experimental and theoretical research on this topic was done by Muhlstein [3] [4] and Dowell [1] [5], respectively. The applied theories enables describing the system's aeroelasticity in the low subsonic and high supersonic domain, but failed by approaching the vicinity of the speed of sound. New numerical computational FSI (Fluid Structure Interaction) methods using Computational Fluid Dynamics (CFD) and Finite Element Methods (FEM) showed themselves capable of closing this gap, as presented by Hashimoto [6]. Therefore, at DLR investigations were done in order to develop numerical tools validated by experimental results [7], from which an excerpt on the Mach number's Influence is shown in the paper at hand. In addition to the validation of numerical approaches, the performed experiments shall give insight in the local and global physical phenomena related to aeroelastic dynamic instability.

The left side of Equation 1 describes the structure by means of a two-dimensional Kirchhoff plate equation [8]. The first term represents the structure's elastic forces and the second one describes the inertia forces depending on the structure's density ρ_s, its thickness h, its Young's Modulus E and the time t. A third term for structural damping is not considered since it is assumed very small compared to the dominating aerodynamic damping. The latter is part of the aerodynamic loads that are represented on the equation's right side by the pressure difference Δp between flow faced and flow averted side of the structure.

$$EJ\left(\frac{\partial^4 d(x,t)}{\partial x^4}\right)+\rho_s(x)h\frac{\partial^2 d(x,t)}{\partial t^2}=-\Delta p(x,t) \tag{1}$$

In order to calculate the aerodynamic loads, a subsonic theory as well as a supersonic theory by Dowell [5] are employed. Equation 2 shows the calculation of the pressure coefficient c_p, which is the pressure difference divided by the dynamic pressure and the excitation amplitude $\hat{A}$. The equation shows a complex pressure coefficient with real part terms $\Re$ and imaginary part terms $\Im$, as indicated by the characters above the equation.

$$\bar{c}_{pM<1} = \frac{1}{\pi}\left[\frac{d^2\psi_n}{dx^2}\right]_{\Re} + j\left[\frac{2\omega}{U_\infty}\frac{d\psi_n}{dx}\right]_{\Im} - \left[\omega^2\frac{\psi_n}{U_\infty^2}\right]_{\Re} \tag{2}$$

Besides the structure's frequency ω ($2\pi f_{exc}$) and the free stream velocity U_∞, the structure's modal shape ψ_n is crucial for the result. Since the phasing between the structure's and the aerodynamic oscillation is responsible for the damping of the system, this paper focuses later on the pressure's imaginary part. With no imaginary part the damping is zero, whereas a positive imaginary part indicates a positive damping and a negative one a negative damping. The latter is required for vreating aeroelastic instability. The theory is only valid for low subsonic Mach numbers $M_\infty < 0.3$ and by using the Prandtl-Glauert transformation even for high subsonic Mach number $M_\infty < 0.7$ [9], [10]. The theoretical approach applied for supersonic flow in Equation 3 is based on the Piston Theory by Ashley [11] and is also described by Dowell [5]. The Equation is composed of the same variables as in the subsonic case, except for the free stream Mach number M_∞. Again, the equation can be divided in real part and imaginary part components. Since the Piston Theory is also a linear theory, the non-linearities occurring in the vicinity of $M_\infty = 1.0$ are not considered and its validity is limited to supersonic Mach numbers $M_\infty > \sqrt{2}$.

$$\bar{c}_{pM>1,n} = \frac{2}{M_\infty}\left[\frac{d\psi_n}{dx}\right]_{\Re} + j\left[\frac{\omega}{U_\infty}\psi_n\right]_{\Im} \tag{3}$$

The one parameter in the equations that needs to be considered in more detail is the structure's mode shape. Figure 2 shows results by Alder [13], where the frequency of the flutter instability is shown as a function of the free stream Mach number.

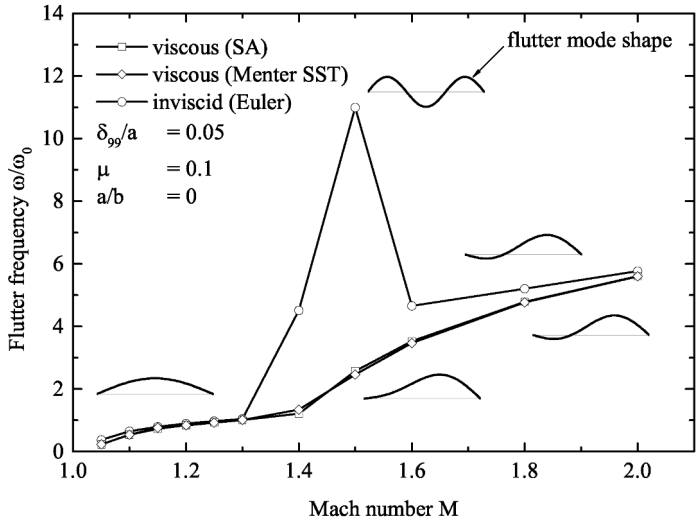

Figure 2 – Aeroelastic instability in low supersonic flow [13].

The Results for viscous flow (*viscous SA*) show the aeroelastic mode shapes and frequencies of for a two-dimensional plate that is simply supported at leading and trailing edge. Considered parameters are the length-to-width ratio *a/b,* the flow boundary layer thickness δ_{99} and the mass ratio μ. The illustrated mode shape are very close to the structure's first modal shape ψ_1 for $1.0 < M_\infty < 1.3$ and an increasing impact of the second mode shape ψ_2 for $1.3 < M_\infty < 2.0$. Derived

from those results is the requirement for the test setup to enable the simulation of the first modal shapes of the test plate. The modal shapes of beams and plates can be calculated analytically by applying an initial function under consideration of the mechanical boundary conditions of the clamped structure [12]. It can also be calculated by a FEM modal analysis as shown in Figure 3.

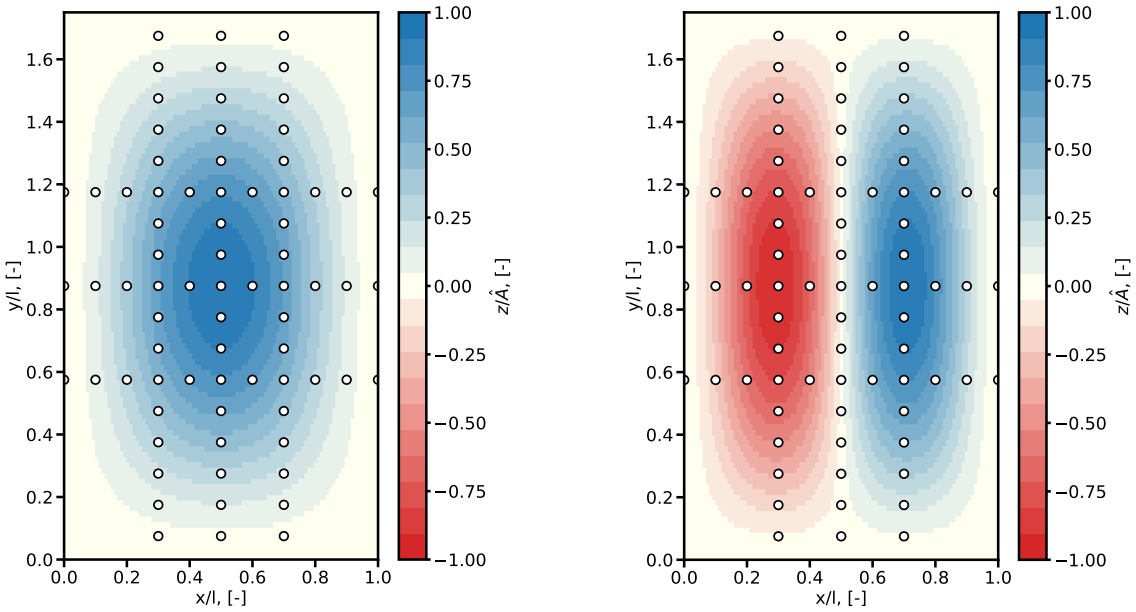

Figure 3 – Modal shapes one (ψ_1) and two (ψ_2) of a flat rectangular plate; FEM calculation.

A test setup able to simulate these shapes can induce the required aerodynamic response. Content of the paper at hand are the measurements in connection with the simulation of the first modal shape. A direct measure for the aerodynamic damping are Generalized Aerodynamic Forces (GAFs), which are directly based on the aerodynamic loads and the involved modal shapes of the structure. According to Equation 4, the GAFs Q_n for a single degree of freedom (1 DOF) system ($n = 1$) can be calculated by multiplying the specific modal shape ψ_n with the pressure difference Δp evoked by that shape.

$$Q_n(x,y,t) = Q_{nn}(x,y,t) = \int_0^w \int_0^l \Delta p_n(x,y,t)\,\psi_n(x,y,t)\,dx\,dy \tag{4}$$

Since the product of pressure and shape is integrated over the plate's length and width, the result is one global value. In case a local observation is needed, only the product of shape and pressure is calculated as a function of x and y giving information on the local state.

2. Experimental Setup

The wind tunnel experiments are based on a forced motion conception, where hydraulic actuators induce harmonically oscillating deformations of the test specimen, which is a flat rectangular panel made of steel. Figure 4 shows a scheme of the test setup in the ψ_1 configuration, which is subject of the paper at hand. A comparison by means of a MAC (Modal Assurance Criterion) approach shows excellent agreement of the calculated first modal shape and the measured deformation (simulated shape) that is evoked by one hydraulic actuator attached to the panel's center (Figure 4 (a) and (b)) [7].

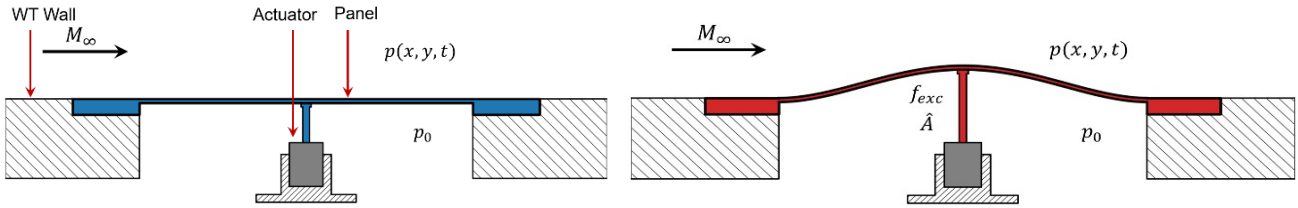

(a) Non-deflected. (b) Deflected.

Figure 4 – Experimental Setup.

With respect to Figure 2, which indicates single mode flutter for $1.0 < M_\infty < 1.2$, the test setup simulates a 1 DOF system that allows exclusively structural motions of the plate's first modal shape ψ_1. The parameters of the test panel deformation are the amplitude $\hat{A}$, which is the actuator's stroke, and the excitation frequency f_{exc}. Both are measured optically by a stereo pattern recognition system (SPR) and additionally by a travel sensor that is integrated in the hydraulic actuator. Figure 5 presents a detailed view on the test structure. The pattern of white markers tracked by the two cameras of the SPR system is shown on the left Figure (sections S_{z1} to S_{z6}), which illustrates a view on the test specimen's flow faced side.

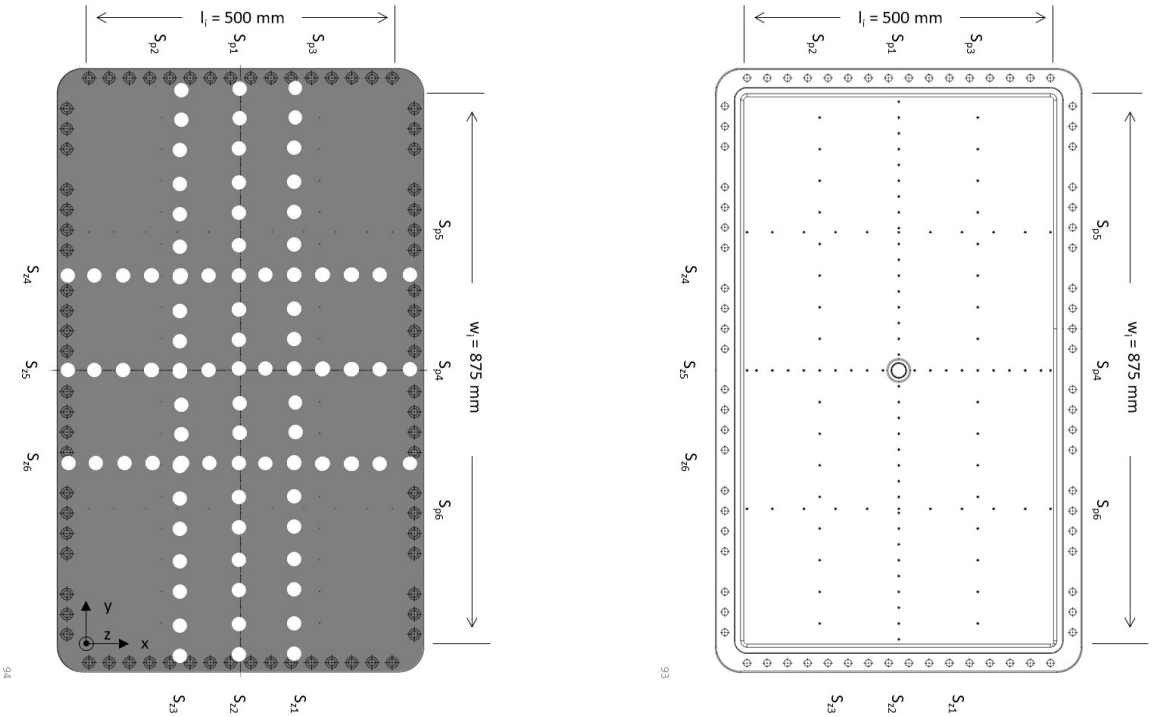

(a) Marker pattern for unsteady deformation measurement (top view).

(b) Pressure sensor positions for unsteady pressure measurement (rear view).

Figure 5 – Test specimen with applied sensor patterns [9].

The applied measurement technique focuses further on the aerodynamic response evoked by the deformations by means of unsteady pressure. That response is measured by highly sensitive and unsteady miniature pressure transducers indicated in Figure 5 (b), which shows the flow averted side of the panel, where the transducers are attached to the depicted orifices. The experiments are carried out in the Transonic Wind Tunnel in Göttingen (DNW-TWG) within a Mach number range of $0.7 < M_\infty < 1.2$ and for three different Reynolds numbers ($Re_1 = 2.5 \cdot 10^6$, $Re_2 = 5.0 \cdot 10^6$, $Re_3 = 7.5 \cdot 10^6$). The main components of the test facility are shown in Figure 6. The rotation speed of the axial compressor (1) as well as the variable diffuser's adjustment (2) control the wind tunnel's Mach number. A pressure chamber (4) enables the wind tunnel for a variation of the total pressure. The test setup is installed in the test section (3) having a cross section of 1m squared.

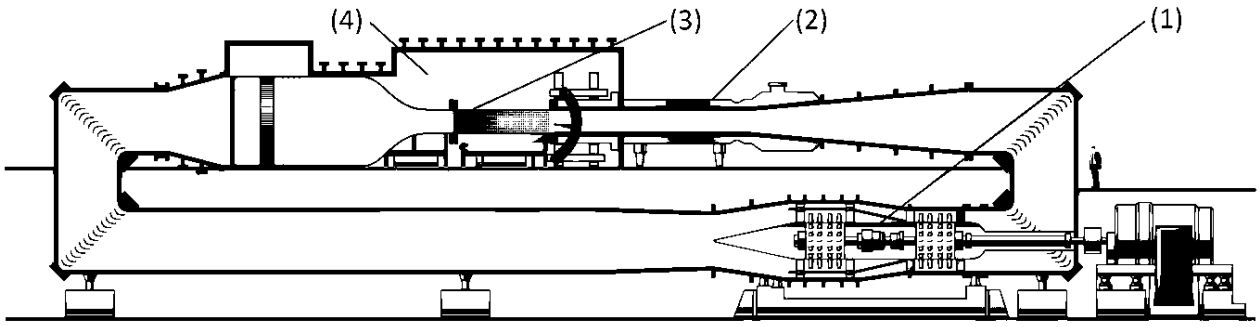

Figure 6 – Transonic Wind Tunnel Göttingen (DNW-TWG, source: DNW).

3. Results

This section illustrates the results of measurements done on the first modal shape tests and in particular on the transition of characteristics of the aerodynamic response by crossing of $M_\infty = 1.0$ from subsonic to supersonic characteristics. Excitation frequency, amplitude and Reynolds number remain constant. As indicated in the preceding section, the pressure data is presented by means of complex values. The reference is the actuator's and thus the structure's motion. Although all components of the complex numbers are shown, at least for the pressure, the focus is drawn on the imaginary part, which indicates the aerodynamic damping. First, illustrations of two-dimensional results ($f(x,y)$) over the entire test structure shall give a general impression on the acquired data. Based on the sections of markers and transducers shown in Figure 5, the data is interpolated and extrapolated over the plate. In the second part only one-dimensional results gained at $y/w = 0.5$ are used for detailed discussion.

3.1 Deformation

Deformation results for different Mach numbers are shown in Figure 7. Since the structure is oscillating completely without phasing to the actuators motion, there is no imaginary part. This means the deformation's real part and its absolute value are equal. The latter is illustrated, which shows at a first glance a good agreement with the calculated modal shape shown in Figure 3. This impression is proven by an excellent outcome of a comparison of the modal shape and the measured shape by using the Modal Assurance Criterion MAC [9].

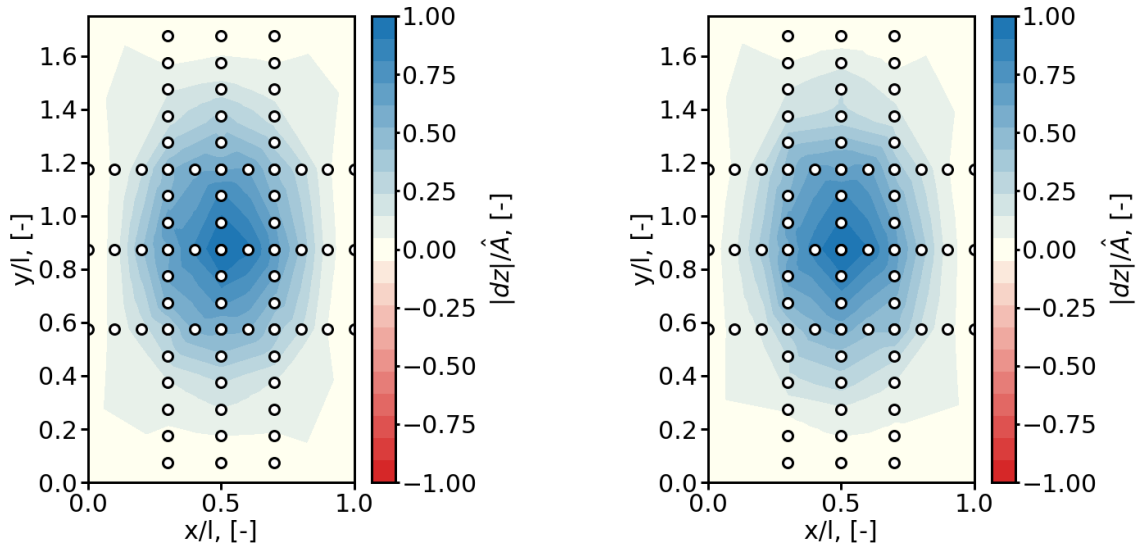

(b) $M_\infty = 0.7$ (b) $M_\infty = 1.2$

Figure 7 – Real part of structural deformation; Influence of excitation frequency at subsonic flow conditions; f_{exc}= *10.0 Hz; Re = 7.5·10⁶;* $\hat{A}$ *= 1.8 mm;* ψ_1 [7].

3.2 Pressure

Representative results of subsonic and supersonic pressure measurements are shown from Figure 8 to Figure 10 by means of the total values of the complex pressure data, the real parts and the imaginary parts. The absolute pressure shows for subsonic flow a characteristic that has lines of symmetry at *x/l = 0.5* and at *y/w = 0.5*. For supersonic flow, the symmetry line at *x/l = 0.5* has vanished. The pressure maximum clearly visible in the panel's center for $M_\infty = 0.7$ has shifted to about *x/l = 0.75 for* $M_\infty = 1.2$.

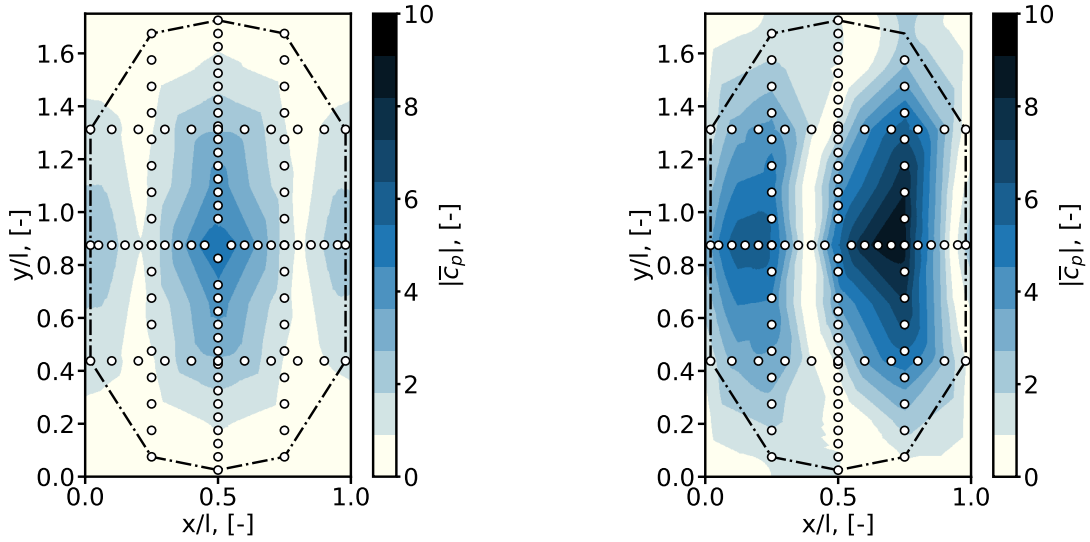

(b) $M_\infty = 0.7$ (b) $M_\infty = 1.2$

Figure 8 – Absolute pressure at subsonic and supersonic flow conditions; f_{exc}= *25.0 Hz;* *Re* = 7.5·10^6; $\widehat{A}_N$ = *1.8 mm,* ψ_1 [7].

In Figure 9, which shows the pressure's real part of the same measurement point, a similar shift occurs. The dominating negative domain with its maximum in the panel's center has moved downstream for supersonic conditions.

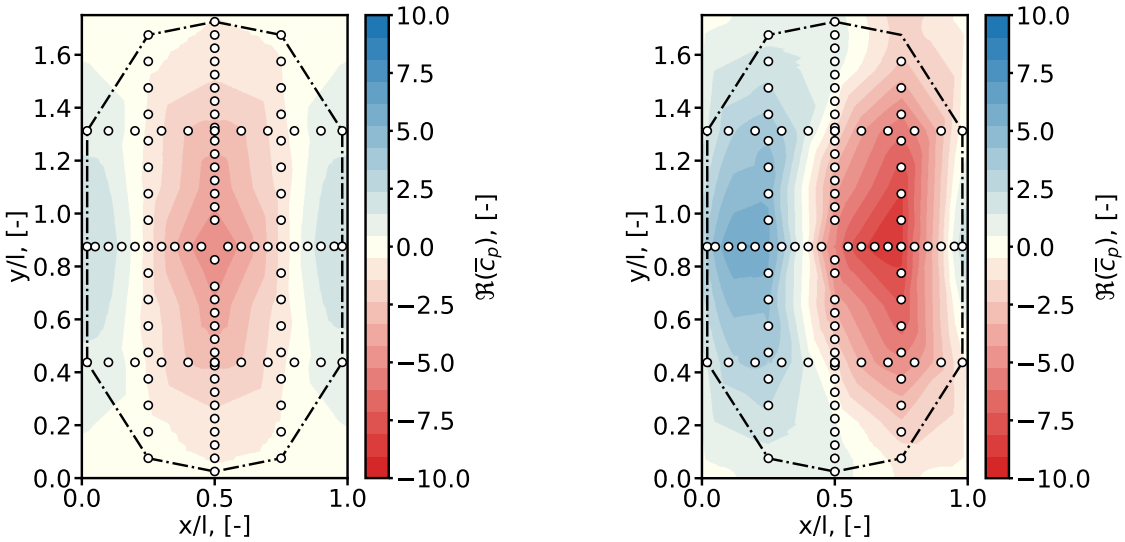

(b) $M_\infty = 0.7$ (b) $M_\infty = 1.2$

Figure 9 – Real part of pressure at subsonic and supersonic flow conditions; f_{exc}= *25.0 Hz*; *Re* = 7.5·10^6; $\widehat{A}_N$ = 1.8 mm, ψ_1 [7].

The pressure's imaginary components shown in Figure 10 do not show the previously made observation of a shift of the characteristics. Here, the impression of a change in algebraic signs from subsonic to supersonic flow is given. With reference to the introductory section, the subsonic results show positive aerodynamic damping for *x/l < 0.5* and a negative damping for *x/l > 0.5*. The other way around are the characteristics shown in Figure 10 (b) for supersonic conditions. After depicting the results over the whole plate, a more detailed presentation along the plate's length at *y/w=0.5* follows in the next sections. This enables a more detailed view for validation purpose and for analyzing the transition happening by passing $M_\infty = 1.0$.

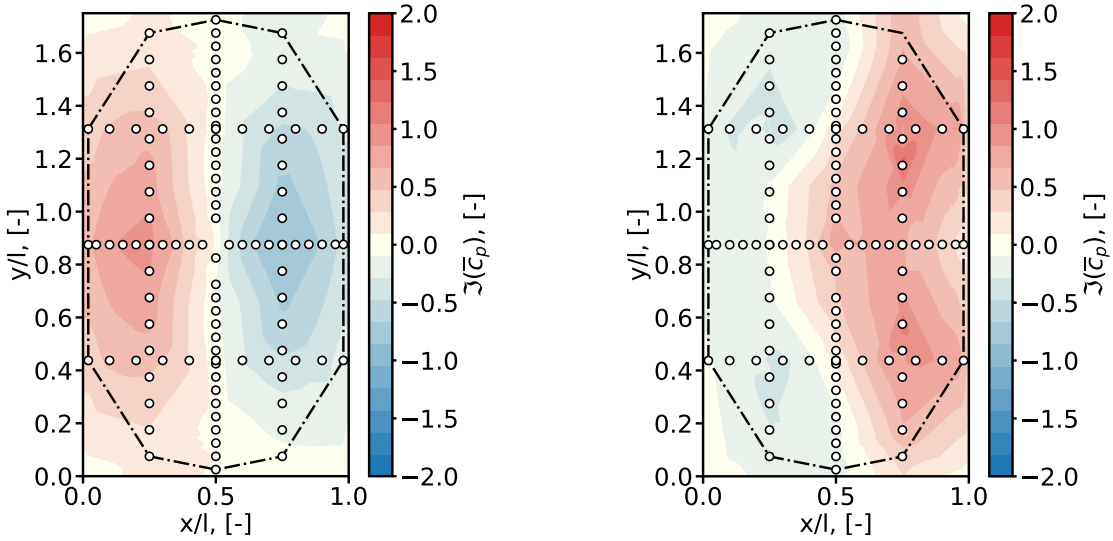

(b) $M_\infty = 0.7$ (b) $M_\infty = 1.2$

Figure 10 – Imaginary part of pressure at subsonic and supersonic flow conditions; f_{exc}= *25.0 Hz; Re = 7.5·10⁶;* $\widehat{A}_N$ *= 1.8 mm,* ψ_1 [7].

3.3 Theoretical references

The results for the complex pressure calculated according to the theories described in Equation 2 and Equation 3 are shown in Figure 11 and Figure 12 for *y/w = 0.5*. On the left side the real part is shown, whereas the imaginary part is presented in the right figure. The filled gray shape in the lower half of each diagram depicts the underlying structural deformation causing the colored pressure curves. For subsonic conditions the pressure's real part is calculated according to Equation 2 and shows a cosinusoidal characteristic which is opposed to the structure's deformation ψ_1. The first term of Equation 2 contains the modal shape's second derivative, which is the dominating real part term.

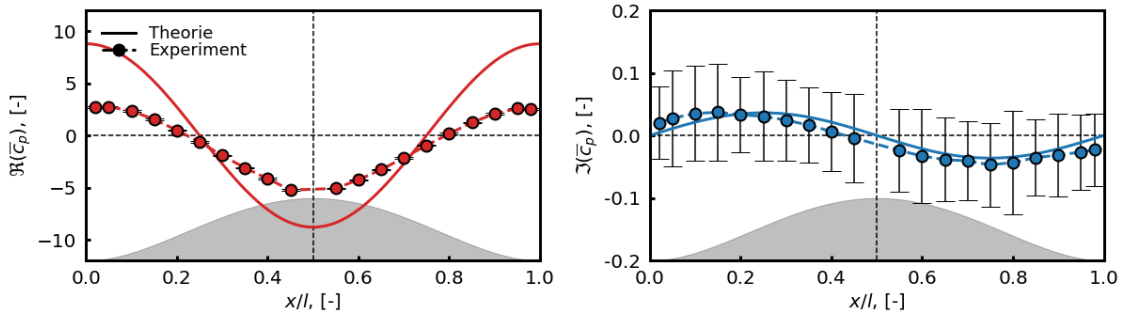

Figure 11 – Pressure; Subsonic theory and measurements; ψ_1, *y/w=0.5,* f_{exc} *= 1.0 Hz,* M_∞ *= 0.7*.

The pressure's imaginary part has a sinusoidal characteristic, caused by the modal shape's first derivative that is contained in the equation's imaginary part term. The added test results meet the characteristics very good. Both the real part's and the imaginary part's characteristic are in agreement

with the theory. The difference in amplitude in the real part can be explained by transverse flows in the real three-dimensional experiments as well as the existence of a boundary layer, which has a damping influence on the pressure's amplitude. The small discrepancies at leading edge and trailing edge for the imaginary pressure results may be caused by imperfections of the plate model, which is supposed to has a curvature of zero at the edges. Figure 9 (a) shows an extensive negative domain in the plate's center and smaller positive domains at the edges, which is also shown in Figure 11. The positive domain in the first half of the panel and the negative one in the second half shown in Figure 10 is also in agreement with pressure's imaginary part in Figure 11.

The theoretical results for supersonic flow show approximately the opposite of the subsonic results. The real part is sinusoidal whereas the imaginary part has a cosinusoidal characteristic. Equation 3 shows that this is in agreement with the rank of derivatives in the two terms for the real and the imaginary components. The positive pressure domain in the first half of the plate and the negative one in the second half for subsonic imaginary pressure appear for supersonic flow for the pressure's real part. The supersonic imaginary part has the cosinusoidal characteristics with a dominating positive domain also shown in Figure 10 (b).

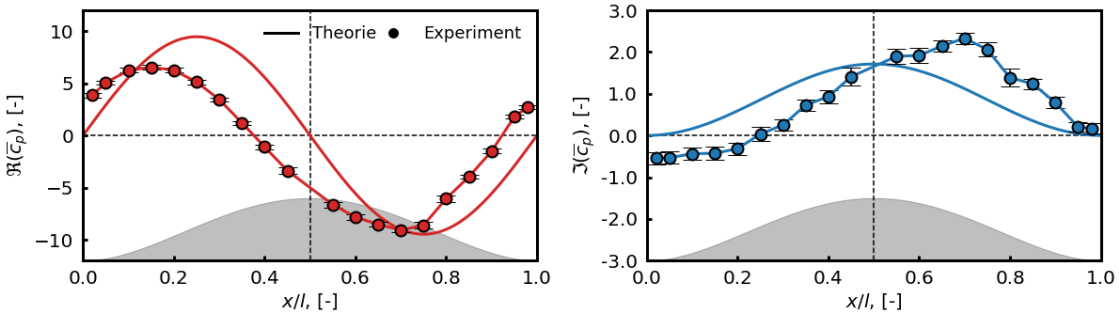

Figure 12 – Pressure; Supersonic theory and measurements for ψ_1, $y/w=0.5$, $f_{exc} = 1.0$ Hz, $M_\infty = 1.2$.

The minimum Mach number established in the measurements is $M_\infty = 0.7$ at which the subsonic equations are just about still valid and the agreement between both is good. For supersonic results the situation is different. The maximum Mach number maintained in the measurements is $M_\infty = 1.2$, where the supersonic theory is just not valid anymore. The agreement is still satisfactory, though no perfect agreement can be expected here. It can be assumed, that test results at higher Mach numbers would show better agreement to that theory.

3.4 Influence of Mach number

The previous section has shown at least plausibility of the measured results and also a change in characteristics from high subsonic flow conditions to low supersonic flow. That transition can not be calculated with the applied theories. Since this change is depending on the Mach number, the next section shows a close examination of the Mach number range in between for two different subsonic Mach numbers at $M_\infty = 0.7$, $M_\infty = 0.95$ and two supersonic Mach numbers at $M_\infty = 1.05$, $M_\infty = 1.2$. Since the overall objective is the observation of damping, only the imaginary parts are considered. In addition the product of the pressure's imaginary part and the structure's deformation is illustrated (see Equation 4), which is a direct measure for local damping.

The pressure shown in Figure 13 (a) for $M_\infty = 0.7$ has characteristics very similar to those depicted in Figure 11 with a positive ($0.0 < x/l < 0.5$) and a negative ($0.5 < x/l < 1.0$) domain. The product of pressure and deformation clarifies those domains being of equal size due to the crossing of the x-axis at $x/l=0.5$. Because of that the resulting integrated GAFs are almost zero. The system has neither a positive nor a negative aerodynamic damping. Results for the second subsonic Mach number, which is close to $M_\infty = 1.0$, are illustrated in Figure 13 (b). Although the characteristics are similar to those observed at $M_\infty = 0.7$, a decisive change occurs. The zero crossing at half-length, at which the

product of pressure and deformation changes from positive to negative, is shifted slightly from *x/l = 0.5* to *x/l > 0.5*. The result is a clearly increased positive domain, both in x-range and in amplitude, and a decrease of the negative domain. The outcome are positive GAFs indicating a positive damping.

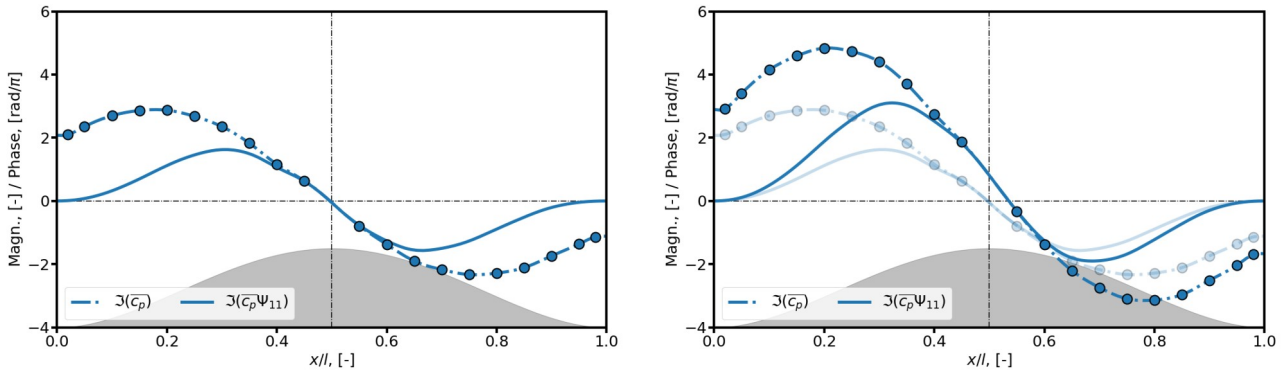

(a) $M_\infty = 0.7$ (b) $M_\infty = 0.95$

Figure 13 – Pressure imaginary part as a function of Mach number; $Re = 5.0 \cdot 10^6$; $\widehat{A}_N = 1.8$ mm, ψ_1, $y/w=0.5$, Subsonic.

At $M_\infty = 1.05$, illustrated in Figure 14 (a), the stream-wise shift of the crossing point of the *x*-axis has increased that leads to a large positive domain and a diminished negative domain. Eventually, Figure 14 (b) shows a product of pressure and shape, which has exclusively positive values for $0.0 < x/l < 1.0$. With each step presented in Figure 13 and Figure 14 the pressure's characteristics are moving from the characteristics calculated by the subsonic theory to those calculated by the supersonic equations. The strongest changes in this transition occur in the vicinity of $M_\infty = 1.0$.

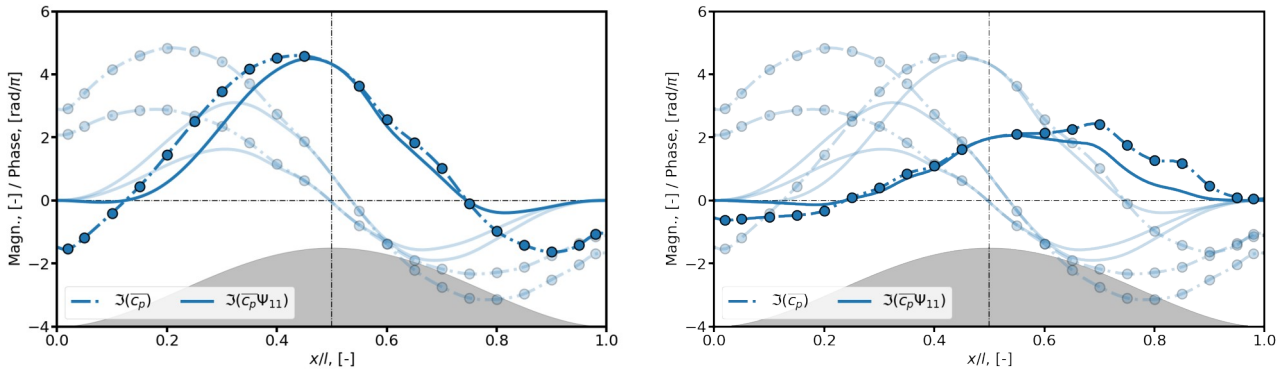

(c) $M_\infty = 1.05$ (d) $M_\infty = 1.2$

Figure 14 – Pressure imaginary part as a function of Mach number; $Re = 5.0 \cdot 10^6$; $\widehat{A}_N = 1.8$ mm, ψ_1, $y/w=0.5$, Supersonic.

4. Conclusions

Wind tunnel tests were performed in order to obtain information on the aerodynamic damping of a flat rectangular plate in high subsonic and low supersonic flow. A 1-DOF system was set up allowing the plate doing motions in its first modal shape ψ_1. A hydraulic actuator forced the structure to undergo those motions in for inducing aerodynamic responses. The structure's oscillating motions as well as the aerodynamic responses (indicated by the complex pressure coefficient) evoked by those motions are measured. Based on those pressure and deformation the system's damping was determined.

A validation with analytic approaches has shown good agreement for high subsonic ($M_\infty = 0.7$) and low supersonic ($M_\infty = 1.2$) flow conditions, whose Mach numbers are also the validity limits of the theories. The focus was drawn on the influence of the Mach number for constant Reynolds number and excitation frequencies. The measured damping characteristics for the Mach number range $0.7 < M_\infty < 1.2$ were analyzed and the transition from subsonic to supersonic characteristics was understood.

Negative global damping was not obtained, which indicates single mode flutter under the tested conditions was unlikely.

In a next step, the also performed tests with a simulated second modal shape ψ_2 are to be discussed and associated with this the possibility of coupled mode instability. Furthermore, the boundary layer's impact, which was not considered, is to be analyzed.

5. Copyright Statement

References

[1] Dowell E. H. *Generalized Aerodynamic Forces on a Flexible Plate Undergoing Transient Motion in a Shear Flow with an Application to Panel Flutter*. *AIAA Journal*, 9(5):834–841, 1971

[2] Sylvester M. A., and Baker E. J. *Some experimental studies of panel flutter at mach number 1.3*. Technical Note 3914, NACA, 1955

[3] Muhlstein L, Gaspers P A and Riddle P D W. *An experimental study of the influence of the turbulent boundary layer on panel flutter*. Technical Note D-5798, NASA, 1968.

[4] Gaspers P A, Muhlstein L, and Petroff D N. *Further experimental results on the influence of the turbulent boundary layer on panel flutter*. Technical Note D-5798, NASA, 1970.

[5] Dowell E. H. *Aeroelasticity of Plates and Shells*. Noordhoff International, Leyden, The Netherlands, 1975.

[6] Hashimoto A., Aoyama T, and Nakamura Y. *Effects on Turbulent Boundary Layer on Panel Flutter*. *AIAA Journal*, 47(12):2785–2791, 2009

[7] Lübker, J. *Aeroelastic Stability of Flat Rectangular Shell Structures in High Subsonic and Low Supersonic Flow*. DLR Forschungsbericht 2020-45, Deutsches Zentrum für Luft- und Raumfahrt e. V., 2020.

[8] Megson T. H. G. *Aircraft Structures for Engineering Students*. Elsevier Ltd., Fourth edition edition, 2007.

[9] Ackeret J. über Luftkräfte bei sehr grossen Geschwindigkeiten insbesondere bei ebenen Strömungen. *Helvetica Physica Acta*, 1 (1928):301–322, 1928.

[10] Glauert H. The Effect of Compressibility on the Lift of an Aerofoil. *Proceeding of the Royal Society A*, 118(779):113–119, March 1927

[11] Ashley H and Zartarian G. Piston Theory: A New Aerodynamic Tool for the Aeroelastician. *Journal of the Aeronautical Sciences*, 23(12):1109–1118, 1956.

[12] Irretier H. *Grundlagen der Schwingungstechnik 2*. Vieweg & Sohn., first edition edition, 2001

[13] Alder M. Development and Validation of a Fluid-Structure Solver for Transonic Panel Flutter. *AIAA Journal*, 53(12):3509–3520, December 2015.